

Substorm injections produce sufficient electron energization to account for MeV flux enhancements following some storms

M. J. Mithaiwala and W. Horton

Department of Physics, University of Texas, Austin, Texas, USA

Received 29 March 2004; revised 9 December 2004; accepted 3 March 2005; published 22 July 2005.

[1] One of the main questions concerning radiation belt research is the origin of very high energy (>1 MeV) electrons following many space storms. Under the hypothesis that the plasma sheet electron population is the source of these electrons, which are convected to the outer radiation belt region during substorms, we estimate the flux of particles generated at geosynchronous orbit. We use the test particle method of following guiding center electrons as they drift in the electromagnetic fields during substorm dipolarization. The dipolarization pulse model electromagnetic fields are taken from the Li *et al.* (1998) substorm particle injection model. We find that a substorm dipolarization can produce enough electrons within geosynchronous orbit to account for the electrons seen following storms. To do this, we compute transport ratios of plasma sheet electrons, that is, the relative ratio of plasma sheet electrons that are transported and trapped in the inner magnetosphere during substorms, as well as the change in energy of the electrons. Since high fluxes of MeV electrons are only seen following storms and not isolated substorms, it is likely that these electrons may serve as a source population for other energization mechanisms which accelerate the electrons to MeV energies. Furthermore, we do parametric studies of the dipolarization model to understand physically what conditions enable the generation of this source population.

Citation: Mithaiwala, M. J., and W. Horton (2005), Substorm injections produce sufficient electron energization to account for MeV flux enhancements following some storms, *J. Geophys. Res.*, *110*, A07224, doi:10.1029/2004JA010511.

1. Introduction

[2] One of the main questions concerning current space weather research is the origin of the relativistic electron radiation belts existing in the dipolar regions of the Earth's magnetosphere. Given that the average electron temperatures of solar and magnetospheric particles are $T_e \sim 10$ eV for the solar wind, 30 eV in the magnetosheath, 500 eV in the plasma sheet, and less than 1 eV in the ionosphere, it is important to ask what is the means that these low-energy electrons come to be energized to 1 MeV and above in the radiation belts. Baker *et al.* [1998] propose that that the process by which high-energy (>1 MeV) electrons are accelerated is twofold: first, there is a prompt acceleration of electrons during magnetospheric substorms and, second, involves other acceleration mechanisms throughout the trapping region (the region in the inner magnetosphere where electrons and ions can drift on closed shells) on a timescale of days. Our focus here is on the first step of this process. The issue of whether the particles come from the solar wind has been addressed in the work of Li *et al.* [1997]. It was determined that the phase space density of solar wind electrons (>20 keV) is not adequate to supply the radiation belts. The plasma sheet is the likely source of

particles. The magnetosheath and ionosphere as sources will not be considered here.

[3] One can ask whether substorms themselves can produce relativistic outerbelt electrons? This question was addressed in the work of Kim *et al.* [2000]. They trace electron guiding center test particles in MHD modeled fields. The MHD fields were meant to simulate a dipolarization process that occurs during substorm onset. The test particle traces showed that plasma sheet electron energies of tens of keV can be transported from $20 R_E$ to $10 R_E$ and can gain about a factor of 10 in energy. When the particles were further transported (by what was assumed to be diffusion) to $6 R_E$ while conserving the first adiabatic invariant, they will have energies of 1 MeV or greater. Estimating the number of source relativistic electrons, they find that only 2% of radiation belt electrons could be accounted for, although this estimate is very sensitive to electron temperature. Ingraham *et al.* [2001] report that the March 1991 storm had intense substorm activity, and velocity dispersion analysis shows that substorms transport not only typical 50–300 keV electrons but also relativistic 0.3 to several MeV electrons to geosynchronous orbit.

[4] Another dipolarization model is the Li *et al.* [1998] model. The main result of this model was that it accurately simulated a dispersionless injection event seen on 10 January 1997. Sarris *et al.* [2002] revised the Li *et al.* [1998] model to make the propagation speed of the time-varying

fields a function of radial distance. This model also reproduced the timing and flux of dispersionless electrons.

[5] We can then ask: “Is the plasma sheet electron population the source of radiation belt electrons? Is there sufficient phase space density? How many electrons can be transported efficiently and under what circumstances?” Since many of the features associated with the Li model have already been published and are known, i.e., dispersionless injections, drift echoes, injection boundaries, the current work reported here is to ask similar questions to *Kim et al.* [2000] and *Ingraham et al.* [2001], i.e., what is the flux of electrons at geosynchronous orbit due to these injections? Is the flux of particles enough to account for the high-energy radiation belt particles created by diffusive processes or other in situ heating processes?

[6] Previously, *Delcourt et al.* [1990] and *Birn et al.* [1998] have investigated electron injections on the basis of test-electron orbits in the dynamic fields of a three-dimensional MHD simulation of dipolarization. They find results in excellent agreement with observations of substorm injections. *Zaharia et al.* [2000] compute electron orbits analytically and also find agreement with observations of substorm electron fluxes.

[7] Recently, an important issue regarding substorm injections is the relation between single large-scale dipolarization pulses with multiple smaller-scale pulses. We note that often there is a series of dipolarizations producing the sawtooth waveform of the injected ion flux. There are many examples of saw tooth injections such as the GEM storm for 4–6 October 2000 submitted for community-wide study. *Ingraham et al.* [2001] propose that strong repetitive substorm injections during the March 1991 storm contributed significantly to the near-record levels of MeV electron fluxes.

[8] We begin by describing the Li et al. dipolarization pulse model, indicating some results that have already been established, followed by simulations of plasma sheet particles. In particular, we reproduce and comment on some of the typical features of observed dispersionless injections. Then we determine the effect of the model parameters of transporting and energizing plasma sheet electrons to the inner magnetosphere, followed by calculations of the flux of electrons generated by substorm injections compared with that seen after a storm.

2. Substorm Dipolarization and Particle Injection

[9] Particle injections at geosynchronous orbit have long been a reliable indicator of substorm onset and have long since been observed [*Arnoldy and Chan*, 1969]. The injections of electrons are often dispersionless in that the flux of soft electrons (<300 keV) are simultaneously enhanced. Although dispersionless ion injections are also observed and may play a very important role in the generation of the ring current [*Kamide et al.*, 1998; *Daglis et al.*, 1999], we do not consider them here.

[10] Two different mechanisms have been proposed for the explanation of these events, a dynamic process such as transport of particles from other spatial regions or penetration by a quasi-static spatial structure [*Kivelson et al.*, 1979]. The dispersionless nature of these injections lead to the “injection-boundary” model, in which a time-

varying spatially localized electric field heats the plasma through convective flow. This belongs in the latter category [*McIlwain*, 1974]. Local spatial energization was thought to be required since energy dependent gradient drifts $\nabla_{\perp} B$ would disperse the plasma spatially according to energy.

[11] *Russell and McPherron* [1973] first reported a compressional pulse associated with dipolarization based on OGO-5 and ATS-1 observations. They suggested that at the expansion phase onset, cross-tail currents weaken and this information is carried across field lines as a compressional wave toward the Earth. Furthermore, they noted that these compressional waves produced “significant betatron acceleration.” The perpendicular flux of particles with 90° pitch angles sharply increased while the parallel flux remained relatively constant. On the basis that the injected plasma is associated with an abrupt increase in the magnetic field, *Moore et al.* [1981] showed that an induced electric field of the compressional wave is responsible for the injected particles.

[12] Substorm injections typically produce energies up to a few hundred (~300) keV [*Cayton et al.*, 1989; *Baker et al.*, 1989]. Furthermore, they typically have a “pancake” pitch angle distribution, that is, the distribution is strongly peaked toward 90° [*Russell and McPherron*, 1973; *Baker et al.*, 1978]. Even the MHD field study of *Kim et al.* [2000] find that only particles near 90° pitch angle are transported to the inner magnetosphere. For these reasons we consider it reasonable to only consider 90° pitch angle electrons but still recognize that it is an approximation.

2.1. Li et al. Model

[13] The Li et al. model is an analytic model for an earthward propagating compressional wave, it is only meant, however, to have the necessary electrodynamics to explain dispersionless injections. However, it can be associated with the phenomenology of substorm onset. In particular, the magnetic field consists of an increase followed by a decrease with the net effect that the magnitude of the field is larger, indicating dipolarization. This increasing field should also correspond to an increased current perpendicular to the plane, indicating the rise of the “substorm current wedge” and the associated decreased cross-tail current of a “current disruption.” The model does not consider a background dawn-to-dusk electric field or the corotation electric field that normally exists in the magnetosphere. The lack of background convection field may preclude any accurate calculation of the fluxes of injected particles associated with substorms; however, the model has been successful in modeling observed particle injections, although adding a dawn-to-dusk electric field increases convection, which would only make the conclusions here much easier to attain.

[14] This model has its origins in a model for the sudden compression of the magnetosphere by an interplanetary shock, in particular that which occurred during the 24 March 1991 SSC [*Li et al.*, 1993]. The electric and magnetic fields associated with dipolarization were originally used to model a shock event which suddenly produced a new radiation belt. *Sarris et al.* [2002] vary the pulse speed with radial distance to demonstrate that dispersionless injections are achievable under low propagation speeds. This model is a

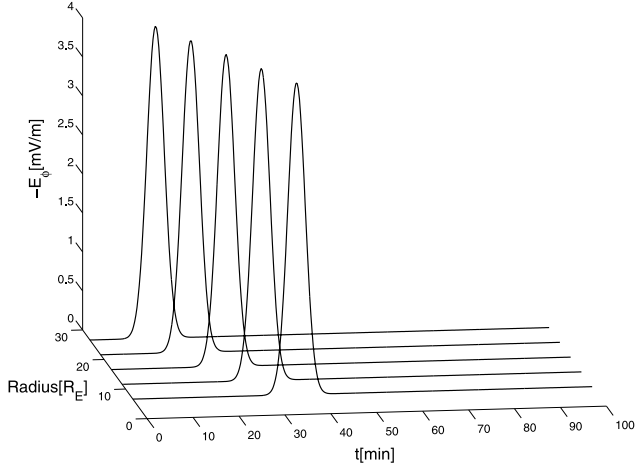


Figure 1a. The electric field is a Gaussian pulse that travels earthward. This figure shows the pulse propagation along the midnight axis. More specifically, each profile represents the electric field that would be seen by a satellite at 6.6, 11.6, 16.6, 21.6, 26.6 R_E . This pulse has parameters $E_0 = 0.5$ mV/m, $v_0 = 100$ km/s, $d = 16,000$ km $\approx 2.5 R_E$, $p = 3$, $A = 1$, $B = 4.0$, $v_d = 100$ km/s, $\phi_0 = 180^\circ$. The maximum field is given by $E_0 2^p = 4.0$ mV/m.

nine parameter model which describes analytic electric and magnetic fields during a substorm dipolarization.

[15] The model fields are most easily derived from the magnetic vector potential

$$A_\phi(r, \phi, \theta = \frac{\pi}{2}) = \frac{dE_0(1 + A \cos(\phi - \phi_0))^p \sqrt{\pi}}{v(r)} \cdot \{ \operatorname{erf}[\xi(r, \phi, t)] + 1 \} \quad (1)$$

using spherical polar coordinates with $\theta = \pi/2$ in the equatorial plane and $\phi = 0^\circ$ is at local noon, positive eastward.

[16] It is useful to define two variables $R_i(\phi)$ and ξ :

$$R_i(\phi) \equiv R_i + \frac{C v(r)}{v_d} (1 - \cos(\phi - \phi_0)), \quad (2)$$

$$\xi \equiv \frac{r - R_i(\phi) + v(r)t}{d}, \quad (3)$$

which are the initial radius of the pulse which depends on the local time ϕ and the location of the peak of the pulse $\xi = 0$.

[17] The Li et al. model pulse parameters are $\{P_i\} = \mathbf{P} = \{E_0, d, p, v_d, v_0, A, C, R_i, \phi_0\}$.

E_0 The amplitude of the electric field;

d $d/\sqrt{2}$ is the radial width of the Gaussian pulse;

p Controls the longitudinal width of the pulse;

v_0 The velocity of the pulse;

v_d Longitudinal pulse velocity;

A Controls the asymmetry between the dayside/nightside amplitude;

C Controls the delay to longitudes away from ϕ_0 or the ratio of v_0 to v_d ;

R_i The initial position of the pulse;

ϕ_0 The modeled electric and magnetic fields are maximum at ϕ_0 .

[18] The electric and magnetic fields are readily obtained:

$$E_\phi = -\frac{\partial A_\phi}{\partial t} = -E_0(1 + A \cos(\phi - \phi_0))^p \exp(-\xi^2) \quad (4)$$

$$B_\theta = [\nabla \times \mathbf{A}]_\theta = -\frac{A_\phi}{r} - \frac{\partial A_\phi}{\partial r} \quad (5)$$

$$= \frac{v'(r)}{v^2(r)} dE_0(1 + A \cos(\phi - \phi_0))^p \frac{\sqrt{\pi}}{2} (\operatorname{erf}(\xi) + 1)$$

$$- \frac{E_0(1 + A \cos(\phi - \phi_0))^p}{v(r)} \left\{ 1 + v'(r) \left(t - \frac{C}{v_d} (1 - \cos(\phi - \phi_0)) \right) \right\} \cdot \exp(-\xi^2)$$

$$- \frac{dE_0(1 + A \cos(\phi - \phi_0))^p \sqrt{\pi}}{rv(r)} \frac{\sqrt{\pi}}{2} (\operatorname{erf}(\xi) + 1).$$

The electric field, Figure 1a, is a Gaussian pulse with electric field vector from the dawn-to-dusk direction. The magnetic field, Figure 1b, shows an overall increase of $|B_\theta|$ simulating a dipolarization event, i.e., an increase in the northward component of the magnetic field. After the transient pulse has passed, the magnetic field is increased by

$$B_\theta = -\frac{d}{r} \frac{E_0}{v(r)} \sqrt{\pi} (1 + A \cos(\phi - \phi_0))^p \quad (6)$$

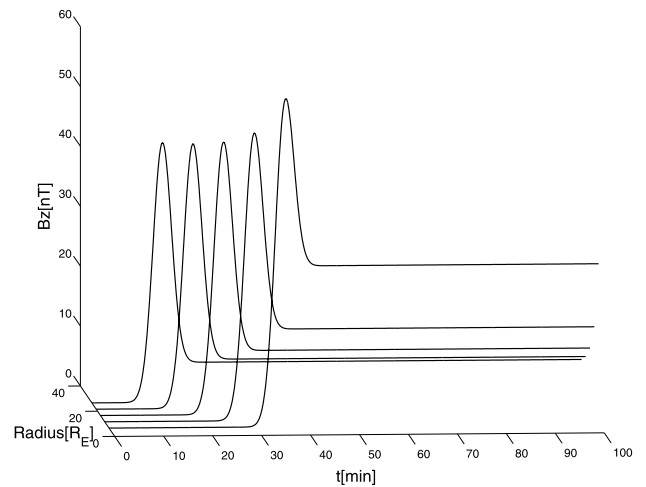


Figure 1b. The dipolarizing magnetic field. This figure shows the pulse propagation along the midnight axis. More specifically, each profile represents the magnetic field that would be seen by a satellite at 6.6, 11.6, 16.6, 21.6, 26.6 R_E . The magnetic field behind the pulse is increased by $\frac{d}{r} \frac{E_0}{v(r)} \sqrt{\pi} (1 + A \cos(\phi - \phi_0))^p$. The $1/r$ dependence explains why the final field is smaller at larger radii.

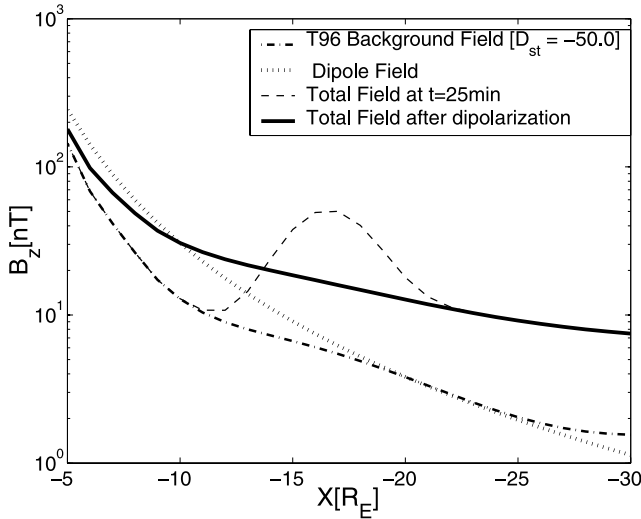


Figure 2. The T96 model is much more realistic in the sense that a simple dipole field is much stronger near the Earth than the T96 model. Here we compare the field strength in the equatorial plane along the midnight axis. The the T96 field with parameters $D_{st} = -50.0$ nT, $P_{dyn} = 3.0$ nPa, $B_z = -3.0$ nT (dash-dotted line), dipole field (dotted line), the field at time $t = 25$ min in cyan, and the total field strength, i.e., T96 background plus model fields (solid line). The field changes from the background field (dash-dotted line) to the intermediate field (dashed line), and the final field (solid line) after dipolarization. The final field is more like a dipole (dotted line) in the inner magnetosphere where we are interested.

when the pulse propagation velocity $v(r)$ is constant. Figure 1b also shows the $1/r$ dependence of the resulting magnetic field.

[19] Further analysis of the field equations, in particular the $(1 + A \cos(\phi - \phi_0))^p$, reveals with $A = 1$ (which is used throughout this article)

$$(1 + A \cos(\phi - \phi_0))^p = 2^p \cos^{2p}((\phi - \phi_0)/2) \approx 2^p \exp\left(-\frac{p}{4}(\phi - \phi_0)^2\right). \quad (7)$$

For this reason, the maximum amplitude of the electric field is really $E_0 \cdot 2^p$. The exponential dependence on $(\phi - \phi_0)^2$ also indicates that the characteristic longitudinal width of the pulse is $2/\sqrt{p}$. A typical substorm current wedge with a 60° angle [McPherron, 1995] would correspond to $p = 14.6$, but we have no evidence that the longitudinal width of the substorm current wedge has any relation to the width of the pulse.

[20] These fields are superimposed upon the Earth's background field (B_E), which is computed using the Tsyganenko 96 (T96) model [Tsyganenko and Stern, 1996]. The T96 model is much more realistic in the sense that a simple dipole field is much stronger near the Earth than the observed field parameterized by the T96 model. Figure 2 shows the strength of the dipole field (dotted line) in the equatorial plane along the midnight axis, the T96 field (dash-dotted line) with parameters $D_{st} = -50.0$ nT, $P_{dyn} = 3.0$ nPa, $B_z = -3.0$ nT chosen to represent a moderately active magnetosphere, and the total field strength (pulse

field plus the background field) after dipolarization is shown with the solid line. The change in overall strength from a depressed background field to a more dipole like field indicates dipolarization. It has been verified that $\nabla \cdot (B_E + B_0) = 0$ and $E_\phi \cdot (B_E + B_0) = 0$.

3. Particle Motion

[21] For the electromagnetic pulse used in these calculations the space scale variation, σ can be estimated by the width of the Gaussian pulse, $\sigma = d/\sqrt{2} \sim 10^7$ m for a width $d \sim 1.5 \cdot 10^7$ and the timescale $\Delta t = \sigma/v_0 \sim 10^5$ s. Considering electron energies in the range of 10 keV to 500 keV found in the magnetotail and magnetic field strengths from 10 nT in the stretched to 200 nT in the dipolar regions (see Figure 2), the gyroradius, $\rho_e = \sqrt{(2mW)/qB}$, of a typical electron decreases from 250 km to 2 km and thus $\sigma/\rho_e > 50 - 1500$ and $\omega_{ce}\Delta t > 10^6$, where $\omega_{ce} = qB/m$ is the electron cyclotron frequency. These large ratios show that it is sufficient to use the guiding-center equations for practical simulations.

[22] The equations of motion are determined by the guiding center equation [Northrop, 1963]

$$\mathbf{v} = \frac{(\mathbf{E} - \frac{\mu}{\gamma_e} \nabla_\perp B) \times \mathbf{B}}{B^2}, \quad (8)$$

where $\gamma = 1 + \frac{\mu B}{m}$ is the relativistic factor and $\mu = p_\perp^2/2mB$ is the first adiabatic invariant or magnetic moment with $\mathbf{B}(\mathbf{x}, t)$ evaluated at the guiding center $\mathbf{x}(t)$. It is essential that these equations retain the Hamiltonian structure of the system [Littlejohn, 1983] in order that Liouville's theorem can be applied to obtain the flux within geosynchronous orbit transported from other regions of the magnetosphere. The guiding-center position \mathbf{x} is given by integration:

$$\mathbf{x}(t) = \mathbf{x}_0(t_0) + \int_{t_0}^t dt' \mathbf{v}(\mathbf{x}(t'), t'). \quad (9)$$

[23] Figure 3a shows two electron orbits under the model fields. Initially, when there is no electric field, the electrons undergo gradient drift motion; the magnetic field gradient is in the negative radial direction ($-\hat{r}$) and the magnetic field direction is out of the plane (\hat{z}) so the resulting motion is toward the dawnside ($\hat{\phi}$). When the magnetic field of the pulse encounters the electron, the gradient reverses and the electrons begin to drift toward dusk ($\hat{\phi}$). The electric field of the pulse is from dusk-to-dawn ($-\hat{\phi}$), so the electron drifts radially toward the Earth during the encounter with the pulse as well. As the pulse passes by the electron, it again begins to drift toward dawn ($-\hat{\phi}$).

[24] The change in particle kinetic energy (W) is given by conservation of the magnetic moment $\mu = W/B$:

$$\Delta W = \mu \Delta B. \quad (10)$$

Figure 3b shows the energy of two electrons during their orbits. As the particles are carried radially inward (Figure 3c), they are energized according to (10).

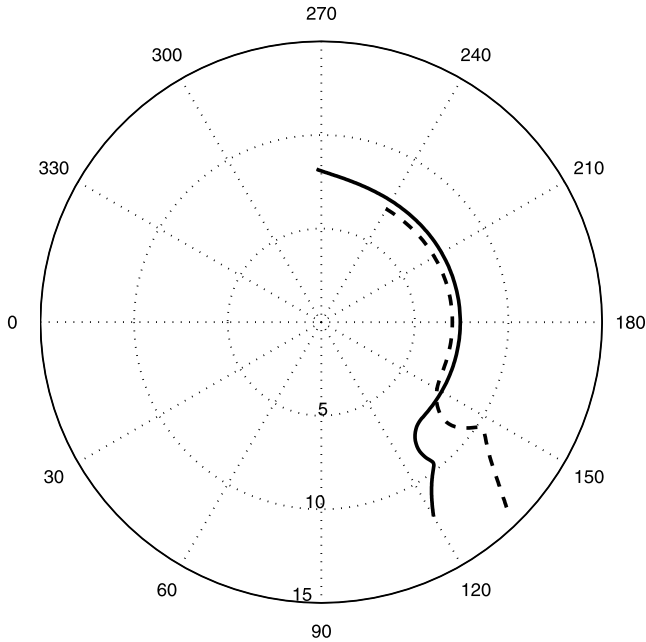


Figure 3a. Two electron orbits with model parameters $\mu = \{E_0 = 0.5 \text{ mV/m}; d = 16,000 \text{ km} \approx 2.5 R_E; p = 3; v_0 = 100 \text{ km/s}; A = 1; B = 0.4; R_i = 40.0 R_E; \phi_0 = 180.0\}$ which are those used in the work of *Li et al.* [1998]. The initial conditions for the orbit are $r_0 = 14 R_E; \phi_0 = 135; W_0 = 25 \text{ keV}; \mu = 1.354 \text{ keV/nT}$ (dashed line) and $r_0 = 12 R_E; \phi_0 = 120; W_0 = 26 \text{ keV}; \mu = 0.9217 \text{ keV/nT}$ (solid line), where μ is the magnetic moment. Initially, when there is no electric field, the electrons undergo gradient drift motion; the magnetic field gradient is in the negative radial direction ($-\hat{r}$) and the magnetic field direction is out of the plane (\hat{z}) so the resulting motion is toward the dawnside ($\hat{\phi}$). When the magnetic field of the pulse encounters the electron, the gradient reverses and the electrons begin to drift towards dusk ($\hat{\phi}$). The electric field of the pulse is from dusk-to-dawn ($-\hat{\phi}$), so the electron drifts radially toward the Earth during the encounter with the pulse as well. As the pulse passes by the electron, it again begins to drift toward dawn ($-\hat{\phi}$).

[25] We comment on the possibility that the magnetic moment, μ , is not conserved. In a low field region, before the arrival of the pulse, when the electron kinetic energy is high, it may be that the magnetic moment is not conserved and the guiding center approximation is invalid. For instance, we use the Tsyganenko field as the background field, see Figure 2, which may not be realistic in the tail regions. If the magnitude of the field were very small and the electron kinetic energy were high enough, this adiabatic condition would not hold. Such a situation could be a reconnection region. However, conservation of magnetic moment is a good approximation for the field model considered here.

[26] We further comment that Figure 2 indicates the background field in the tail is of the order of a few nT. It should then be noted that the energization is very sensitive to the initial strength of the field. A larger field in the tail would produce less energization than a smaller field due to equation (10).

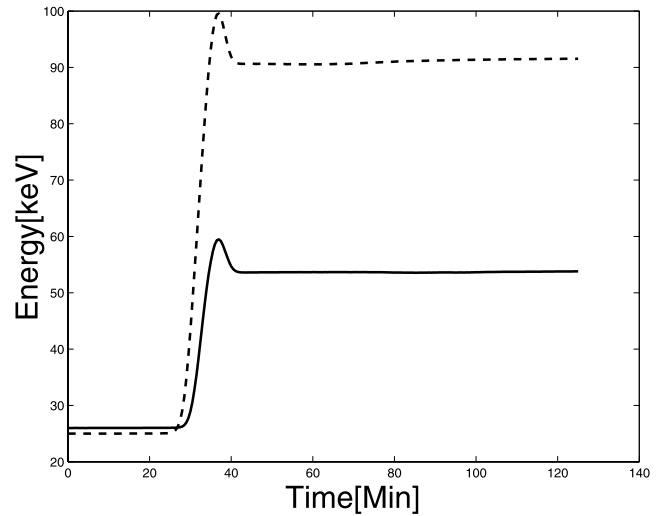


Figure 3b. The energy of the electrons shown in Figure 3a. As the electrons encounter the pulse field they are carried along via drifts (8). The greater the change in magnetic field strength, the greater the energization due to conservation of the magnetic moment. In this case, the electron indicated by dashed line has magnetic moment $\mu = 1.354 \text{ keV/nT}$ and the solid line $\mu = 0.9217 \text{ keV/nT}$. Thus the dashed line electron can gain more energy for that same change in magnetic field ΔB .

3.1. Physical Interpretation of the Effect of Parameters on Single Electron Motion

[27] In this section we comment on the effect of changing the parameters of the fields on the motion of single electron orbits. This will be useful later in understanding the parametric changes for large ensembles of electrons in section 4.

[28] Here, as well as in section 4, we consider variations of the following pulse parameters: $E_0, v_0, p, d, C,$ and R_i . The ranges used, as well as explanations of the values

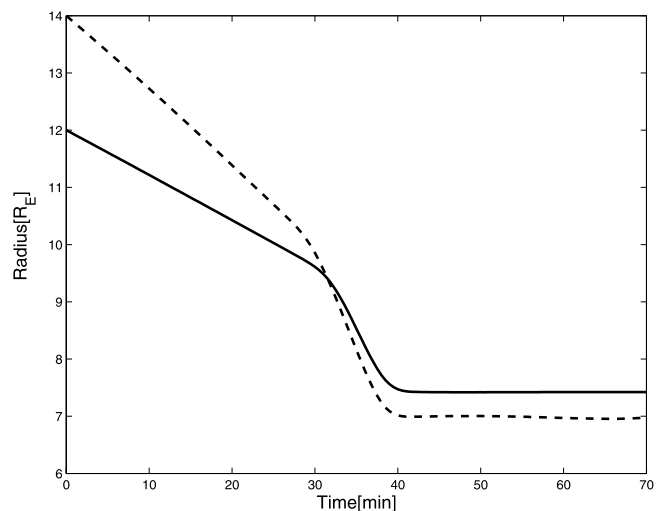


Figure 3c. The radial position of two electrons during their orbit. As the electrons are carried into larger magnetic fields, they gain energy, as indicated in Figure 3b.

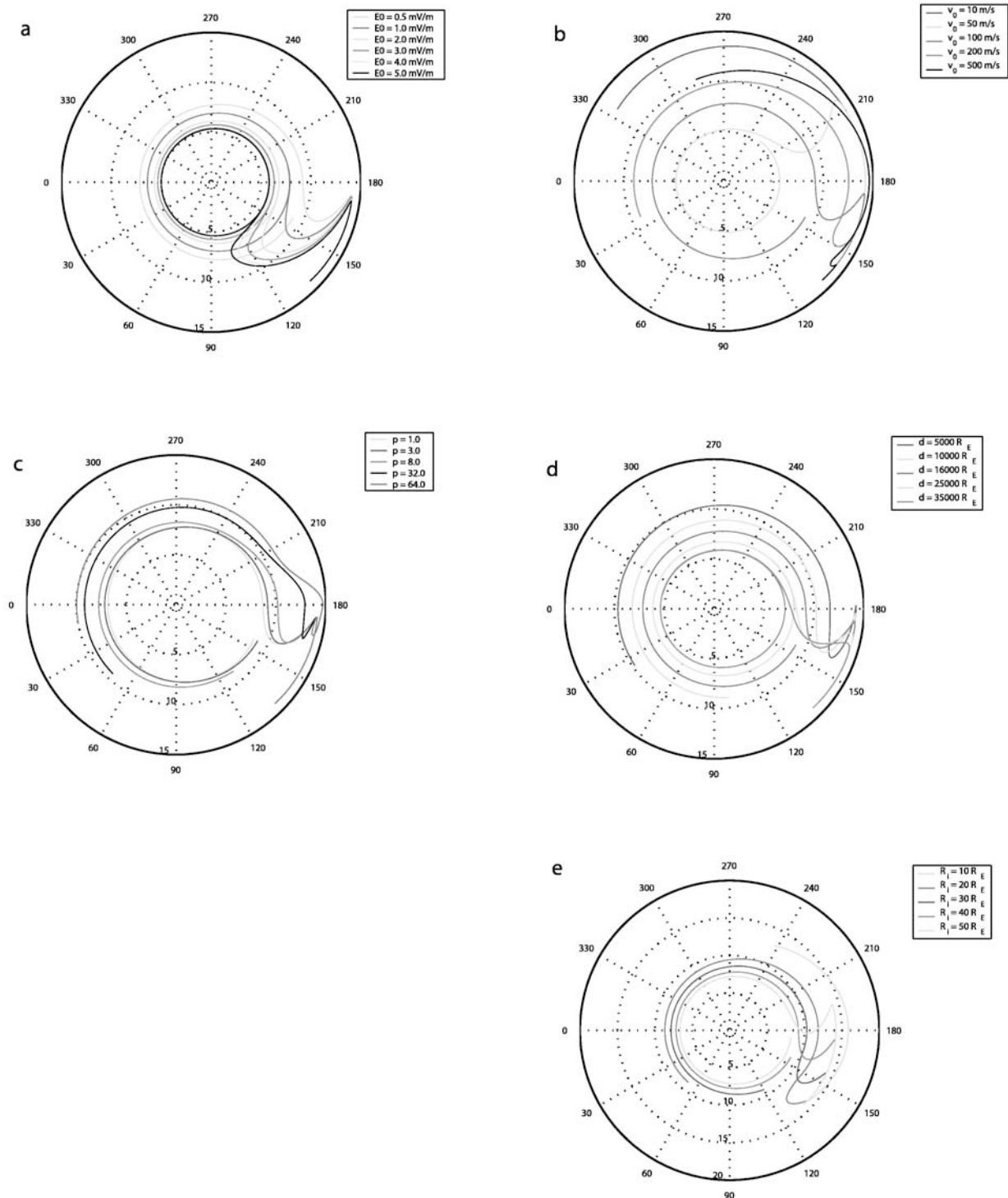


Figure 4. The electron orbit under different variations of the pulse parameters. The electron orbits are computed for pulse parameters of $\mathbf{P} = E_0 = 0.5$ mV/m, $d = 16,000$ km $\approx 2.5 R_E$; $p = 3$; $v_0 = v_d = 100$ km/s; $A = 1$; $C = 0.0 R_E$; $R_i = 40.0 R_E$; $\phi_0 = 180.0$ as baseline parameters, while varying each of the other parameters separately. See color version of this figure at back of this issue.

chosen, are given in section 4.1. The background magnetic field for this section is a dipole field because the motion is easier to compare for the different parameters. Later we use the more realistic Tsyganenko model.

[29] Figure 4a shows the electron orbit under different magnitudes of the electric field. With a stronger electric field, the electron can gain more energy and will be transported inward further than with a weaker electric field. In

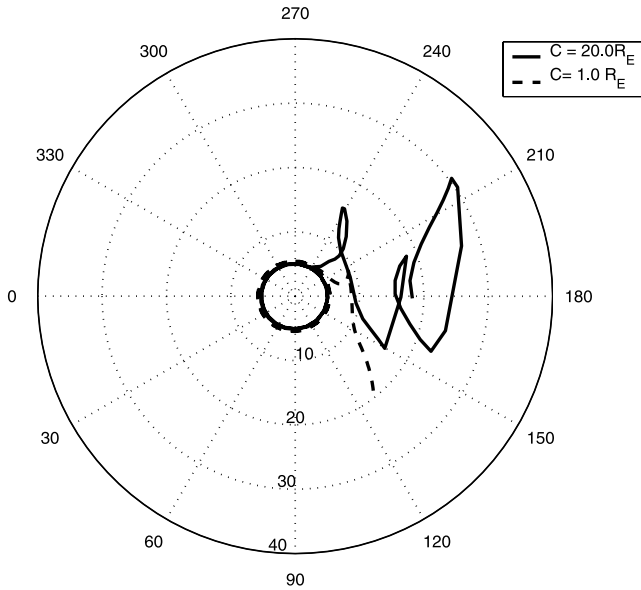


Figure 4f. The electron orbit under different magnitudes of the azimuthal velocity. The electron orbit indicated with the dashed line for parameter $C = 1.0 R_E$ and the solid line for $C = 20.0 R_E$. All other parameters remain constant at $\mathbf{P} = E_0 = 0.5$ mV/m; $v_0 = v_d = 100.0$ km/s; $R_i = 40.0 R_E$; $d = 16,000$ km $\approx 2.5 R_E$; $p = 3$; $A = 1$; $\phi_0 = 180.0$. Because the pulse is greatly delayed at longitudes away from 180° , the solid line electron ($C = 20.0 R_E$) orbit is much more complex than the other orbit. As the electron drifts to longitudes away from 180° , it can interact with the pulse that is delayed to these longitudes. The electric field seen by the electrons is shown in Figure 4g.

addition, during the interval when the electron's drift is reversed, the electron will drift farther in the dusk direction.

[30] Figure 4b shows the electron orbit under different magnitudes of the velocity of the pulse. The orbit labeled with $v_0 = 500$ m/s has very little interaction with the electric field because it moves by so quickly; hence its drift reversal and radial transport is very small. With a smaller velocity, for example $v_0 = 50$ m/s to 200 m/s, the electron interacts with the electric field longer and can drift radially inward better. With a very slow field, the electron drifts azimuthally away and does not interact strongly with a large electric field.

[31] Figure 4c shows the electron orbit under different magnitudes of the longitudinal width, controlled by the parameter p . Large p corresponds to a small width and a small p corresponds to a large width. For orbits labeled with $p = 32$ and $p = 64$, the resulting orbit has a bit of a kink between 180° and 210° . This is a result of the electron drifting azimuthally out of the electric field. With larger pulse widths, i.e., $p = 1.0, 3.0, 8.0$, this does not occur because the pulses are very wide. Naturally, the wider pulses transport electrons inward further because of the longer interaction with the electric field.

[32] Figure 4d shows the electron orbit under different magnitudes of the radial width, controlled by the parameter d . Larger d correspond to larger widths and vice versa. The effect is clear, larger widths correspond to a longer interaction with the fields and hence a better inward transport.

[33] Figure 4e shows the electron orbit under different initial positions of the pulse. When the pulse starts very far earthward, i.e., $R_i = 10 R_E$, there is no opportunity for the electron to interact with the pulse fields. Otherwise, changing the initial position shows that having the pulse start further back is better at transporting the electron earthward; however, this shows only one initial condition.

[34] Figure 4f shows the electron orbit under different magnitudes of the azimuthal velocity. A larger value of C means that the pulse is delayed to longitudes away from 180° . An electron drifting across many different longitudes has the opportunity to see many different peaks in the electric field, as in Figure 4g. So for larger C , the motion can be very complicated.

[35] The results indicate what should be physically clear. The longer the electron can stay in the fields, the better it will be at gaining energy. To get an accurate picture of what happens during a substorm, we must consider larger numbers of electrons with a wide range of initial conditions. We do this in section 4.

3.2. Electron Orbits and Electron Fluxes

[36] In the orbit simulations we use the GSM coordinates and integrate (8) and (9) directly. For understanding the implications of the simulations for the phase space density f and particle flux J , it is clearer to use canonical coordinates and the Hamiltonian structure of the guiding-center equations. The standard canonical coordinates for the dynamics are the magnetic flux ψ and the longitudinal angle ϕ . Transforming from x, y to ψ, ϕ , the dynamics are given by

$$\frac{df}{dt} = \frac{\partial f}{\partial t} + [f, H] = 0, \quad (11)$$

where $[H, \cdot]$ is the directional derivative (Lie derivative) along the ψ, ϕ orbits

$$\frac{d\psi}{dt} = -\frac{\partial H}{\partial \phi} \quad \frac{d\phi}{dt} = \frac{\partial H}{\partial \psi} \quad (12)$$

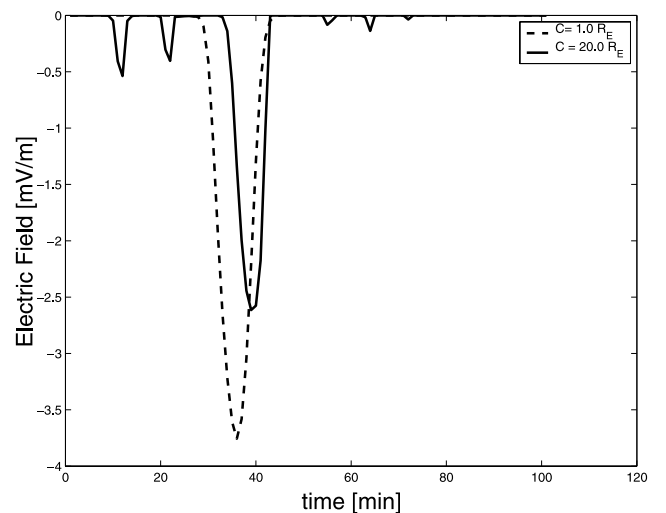


Figure 4g. The electric field as seen by the electrons in Figure 4f. Because the pulse is greatly delayed to longitudes away from 180° with $C = 20.0 R_E$, the solid line ($C = 20.0 R_E$) electron sees a strong electric field many times in its orbit.

and

$$H = \mu B(\psi, \phi, t) \quad (13)$$

is the Hamiltonian for the flow in the equatorial plane. Clearly, it is the broken symmetry from the ϕ -dependence of the electromagnetic pulse that brings the electrons into the inner magnetosphere.

[37] The magnetic field B is given in Clebsch form of $\mathbf{B} = \nabla\psi \times \nabla\phi$; ψ and ϕ label a field line and s is the coordinate along the field line. Similarly, the magnetic field is given by $\mathbf{B} = B d\mathbf{r}/ds$. Each guiding-center orbit represents an ensemble of a very large number of electron orbits in a finite domain (at least $\pi\rho_e^2$ and often much larger) of the equatorial plane. Every area $\Delta\psi\Delta\phi$ is conserved by the Hamiltonian flow in equations (11)–(13). The inverse Jacobian transformation

$$\frac{1}{J} = \left| \frac{\partial(\psi, \phi, s)}{\partial(x, y, z)} \right| = |\nabla s \cdot \nabla\psi \times \nabla\phi| = |\nabla s \cdot \mathbf{B}| = B. \quad (14)$$

Thus the physical area $\Delta x\Delta y$ of a group of electrons around each guiding-center orbit is compressed by $(\Delta x\Delta y)_{t_f} = \Delta\psi\Delta\phi/B_f = (B_i/B_f)(\Delta x\Delta y)_{t_i}$ in the transport from t_i to t_f , since the Jacobian transformation $|\partial(x, y, z)/\partial(\psi, \phi, s)| = 1/B$ (14). Assuming no electrons are lost, then the invariance of f means that the line density per unit area $\Delta x\Delta y$ increases by (B_f/B_i) in the transport to the inner magnetosphere for the group of electrons in the kinetic energy range $(W_i, W_i + \Delta W_i)$, where $W_i = \mu B_i$. This gives the standard relation $j_f = (p_f/p_i)^2 j_i$ [Lyons and Williams, 1984, p. 21], which expresses conservation of phase space density. Their final speed, however, is dominated by $v_\perp = (\mu B_f)^{1/2}$ and not the guiding center velocity \mathbf{v} from (8). So the particle flux measured by a detector in the inner magnetosphere is $j_f = (B_f/B_i)j_i$ greater than the initial particle flux j_i . By the relation $W = \mu B$ (10),

$$j_f = (W_f/W_i)j_i. \quad (15)$$

[38] Including the compression of the flux tube along the length s of the magnetic flux tube increases the λ exponents of the compression factors $(B_f/B_i)^\lambda$. Now we consider some typical estimates implied by the simulations. Assuming a trajectory from the simulations that takes the bundle of neighboring electrons along $\psi(t)$, $\phi(t)$ to the inner magnetosphere to orbits with $R \sim 5$, we estimate that the line density increases by $B_f/B_i \sim 250 \text{ nT}/10 \text{ nT} = 25$.

[39] The particle flux is increased by greater than 100 and less than 500. To reduce the uncertainty in the range of the enhancement factors requires assumptions about the degree of stretching of the magnetic field lines due to cross-tail current ΔI_{gt} enclosed between the initial and final field lines ($\ell_f B_i \cong \ell_f B_f + \mu_0 \Delta I_{gt}$) and the pitch-angle distribution of the high-energy electron velocity distribution.

4. Multiparticle Simulation

[40] Ensembles of electrons can be integrated in order to compare results with satellite observations and previous

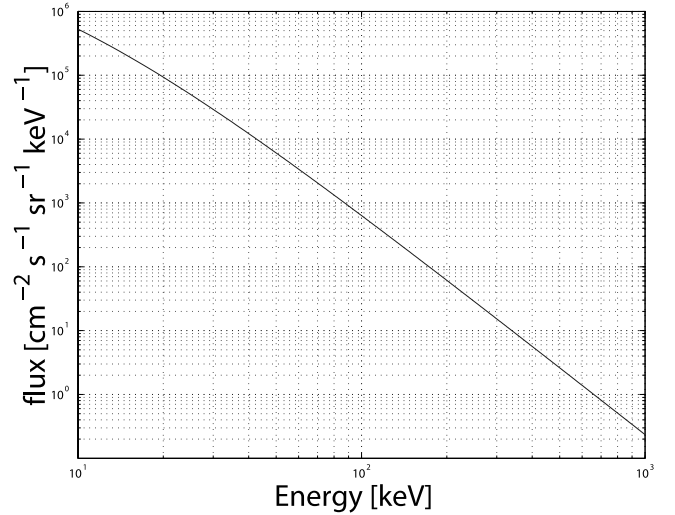


Figure 5. The initial flux of magnetic tail particles is modeled by a kappa distribution (16). We have chosen the parameters as *Kim et al.* [2000] with $\kappa = 3.5$, $E_\kappa = 1.14 \text{ keV}$ and $j_0 = 5.5 \cdot 10^6 \text{ cm}^{-2} \text{ s}^{-1} \text{ sr}^{-1} \text{ keV}^{-1}$.

studies. Here we distribute electrons in the equatorial plane from $7.5 R_E \leq r \leq 20 R_E$ in increments of $0.1 R_E$, $0^\circ \leq \phi < 360^\circ$ in increments of 1° , and energies from $1 \text{ keV} \leq W \leq 512 \text{ keV}$ in increments of 1 keV. This corresponds to the integration of 2,322,4320 electrons. Parallel computer code allows the simulation to be done swiftly. The lower radial bound was chosen as greater than $7 R_E$ since our virtual detectors begin at $6.8 R_E$. These ranges were chosen as to be similar to the simulation of *Li et al.* [1998]. The dipolarization field parameters are also those of *Li et al.* [1998], namely $E_0 = 0.5 \text{ mV/m}$, $v_0 = 100 \text{ km/s}$, $d = 16,000 \text{ km} \approx 2.5 R_E$, $p = 3$, $A = 1$, $B = 4.0$, $v_d = 100 \text{ km/s}$, $\phi_0 = 180^\circ$.

[41] The initial electron distribution in the tail is given by a generalized maxwellian or kappa distribution [Vasyliunas, 1968]

$$j = j_0 \frac{(1 + 1/\kappa)^{1+\kappa}}{E_\kappa} \frac{W}{(1 + W/\kappa E_\kappa)^{1+\kappa}}, \quad (16)$$

with $\kappa = 3.5$, $E_\kappa = 1.14 \text{ keV}$ and $j_0 = 5.5 \cdot 10^6 \text{ cm}^{-2} \text{ s}^{-1} \text{ sr}^{-1} \text{ keV}^{-1}$ [Christon et al., 1991]. We have chosen the parameters as *Kim et al.* [2000]. These parameters represent a harder spectra that is observed during active conditions. Figure 5 shows the initial flux as would be measured by a satellite in the tail region.

[42] By examining the arrival time of the electrons, we determine that the particles that show appreciable energy gains coincide with the arrival of the dipolarization pulse (Figure 6). Figure 8 shows the initial location of these electrons as well as the location of the virtual satellites used as detectors. In keeping with other studies [Li et al., 1998] of a similar nature, we do include a radial dependence in the distribution,

$$f = \left[\frac{(r_0 - a_0)^{nl}}{r_0^{ml}} \right] / \left[\frac{(a_{0d} - a_0)^{nl}}{a_{0d}^{ml}} \right] \quad (17)$$

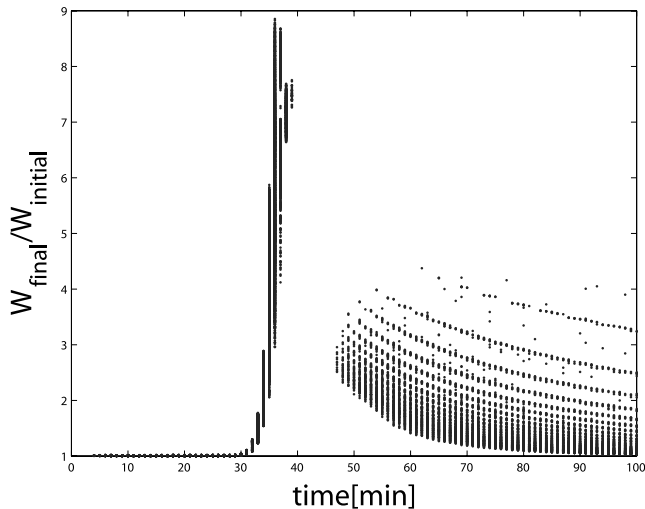


Figure 6. The energization (final energy divided by initial energy) as a function of time. It is clear that those electrons gaining the most energy are coincident with the arrival of the dipolarization pulse at the detectors. The detectors are indicated by black squares in Figure 8.

and $f = f * \exp(-r_0^2/7.5^2)$ when $r_0 > 12 R_E$. The parameters are $a_0 = 3$, $nl = 4$, $ml = 10$, and $a_{0d} = 6$. The electrons are given a weighting according to this function which is shown in Figure 7.

[43] Figure 9 shows the electron flux for the energy channels 105–150, 150–225, and 225–315 keV. These were chosen to be representative of LANL observations of injections reported by *Li et al.* [1998]. The simultaneous flux enhancement across different energies is the key feature of dispersionless electron injections. Similar results were obtained by *Li et al.* [1998]. However, in our simulation we do not include a background flux that would normally be measured by a satellite in the magnetosphere but do include a radial dependence as indicated by equation (17) and Figure 7. This background is typically 10^2 – $10^3 \text{ cm}^{-2} \text{ s}^{-1}$

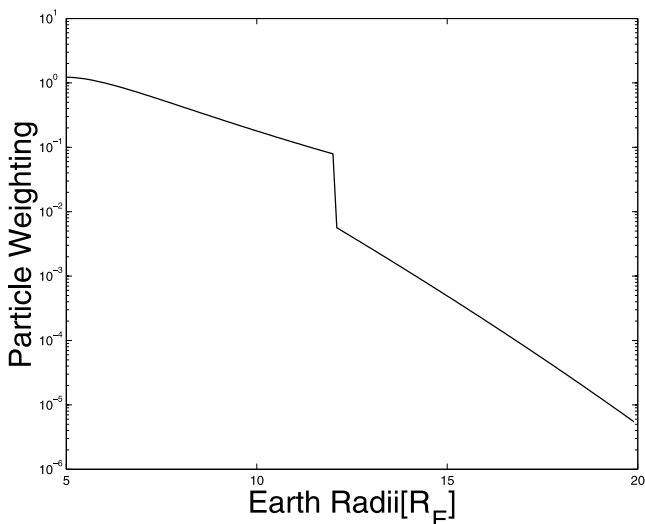


Figure 7. The electrons are weighted according to the initial radial distribution from equation (17).

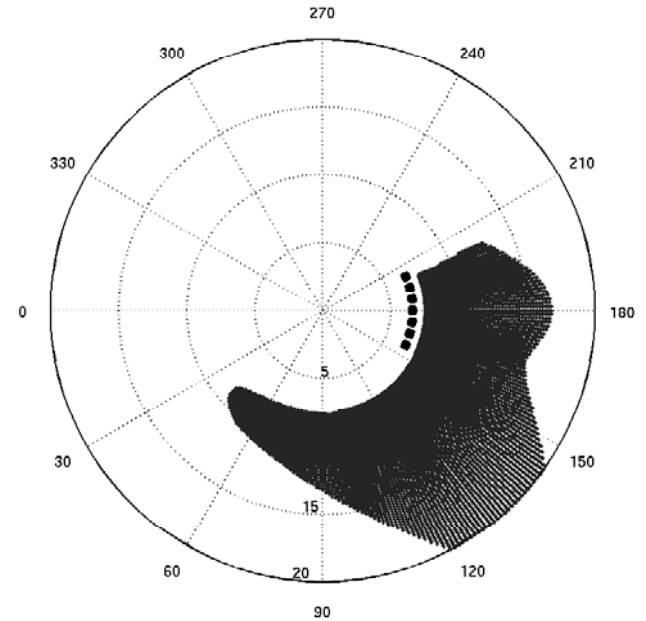


Figure 8. The initial spatial region of electrons was $7.5 R_E \geq r \geq 20 R_E$ in increments of $0.1 R_E$, $0^\circ \leq \phi < 360^\circ$ in increments of 1° , and energies from $1 \text{ keV} \geq W \geq 512 \text{ keV}$ in increments of 1 keV . Here we show the initial location of electrons that were detected by the virtual satellites that are indicated by black squares. There are seven virtual detectors placed at $6.6 \pm 0.2 R_E$ at local times from 2100 to 0300 LT.

$\text{sr}^{-1} \text{ keV}^{-1}$, whereas our initial level is 10^0 – $10^1 \text{ cm}^{-2} \text{ s}^{-1} \text{ sr}^{-1} \text{ keV}^{-1}$. This initial level is due to electrons randomly drifting into our virtual detector. We simply show that the magnitude of the flux achieved by this simulation is that which is typically seen during substorm injections, i.e., 10^3 – $10^4 \text{ cm}^{-2} \text{ s}^{-1} \text{ sr}^{-1} \text{ keV}^{-1}$. We further point out that we do not include effects of detector resolution or other electron loss processes after the injection.

4.1. Results of Further Simulations and the Substorm Injection Flux

[44] Conservation of phase space density, or Liouville's theorem, it is clear that electrons with energies less than 100 keV have sufficient phase space density to account for typical MeV electron fluxes [*Kim et al.*, 2000; *Ingraham et al.*, 2001]. However, it is unreasonable to assume that all these electrons can be convected to geosynchronous orbit. Since in our simulation, an electron placed in the tail field will undergo energy-dependent $\nabla_{\perp} B$ drift out of the tail and hit the magnetopause, this occurs for a large number of electrons in our simulation, particularly the higher-energy electrons.

[45] In other simulations we varied the parameters and integrated a tail distribution of electrons. The purpose of this study is twofold: to determine the influence of the model parameters on energization and transport of particles from the tail during substorm injections and to determine the flux of electrons that would enter geosynchronous orbit in order to be further energized to MeV and higher energies.

[46] Orbits are computed with one-dimensional parameter scans for the parameters listed below in the Table 1.

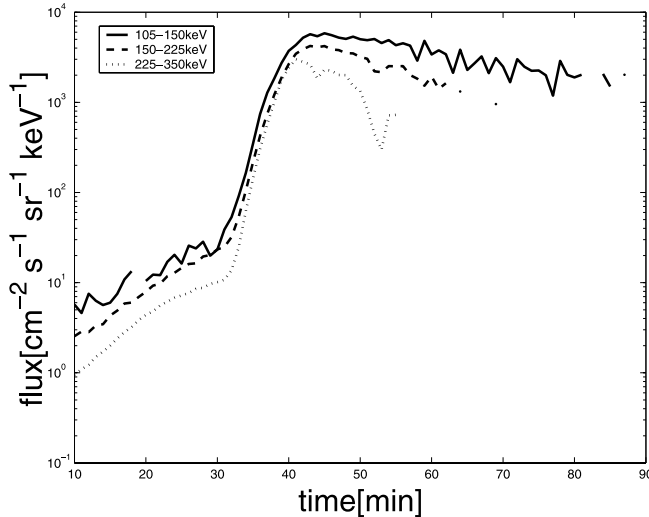


Figure 9. We show that the magnitude of the flux achieved by this simulation is that which is typically seen during substorm injections, i.e., 10^3 – 10^4 $\text{cm}^{-2} \text{s}^{-1} \text{sr}^{-1} \text{keV}^{-1}$. The electron flux for the energy channels 105–150, 150–225, and 225–315 keV. These were chosen to be representative of LANL observations of injections reported by *Li et al.* [1998]. At the approximate time of $t = 33$ min of our simulation, we see the simultaneous enhancement of the flux across different energies. We include a radial dependence as indicated by equation (17) and Figure 7. We point out that we do not include effects of detector resolution or other electron loss processes after the injection.

Namely, we vary each of these six parameters individually while holding the remaining parameters fixed with the reference model values of $E_0 = 0.5$ mV/m, $v_0 = v_d = 100$ km/s, $d = 16,000$ km $\approx 2.5 R_E$, $p = 3$, $A = 1$, $C = 0.0 R_E$, and $\phi_0 = 180^\circ$. These reference values are taken from *Li et al.* [1998], with the exception of the parameter C .

[47] The parameter ranges were chosen for a variety of reasons. The electric field parameter, E_0 , was chosen between 0.5 mV/m and 5 mV/m because measurements indicate an electric field amplitude of 1–50 mV/m. According to (7), the maximum electric field amplitude would be between 4 mV/m and 40 mV/m for $p = 3$. Various experimental determinations have been made; *Moore et al.* [1981] indicate an electric field of 1–10 mV/m; recently, *Fairfield et al.* [1998] reported 50 mV/m; and there have been other measurements made in between as well [*Shepherd et al.*, 1980; *Aggson et al.*, 1983]. It follows that with $E_0 = 5.0$ mV/m and p greater than 4, the electric field amplitude is wildly out of the experimentally observed range. For this reason, during parameter scans in which p is varied, we compensate by normalizing the electric field amplitude to 4.0 mV/m.

[48] There are measured constraints on the velocity as well. Originally, *Russell and McPherron* [1973] reported a velocity of 150 km/s. *Moore et al.* [1981] report a velocity between 10 and 100 km/s. On this basis we choose a broad range of velocities between 10 and 500 km/s.

[49] We have shown earlier that the characteristic longitudinal width of the pulse is $2/\sqrt{p}$. For p in the range of 1.0

and 64.0, the longitudinal width varies from 230° to 30° . Although we state that $p = 14.6$ would correspond to the width of the substorm current wedge, this is not an observational constraint on the width of the pulse.

[50] Observations show that there is very little delay in the arrival of the wave front between satellites that are separated azimuthally but not radially [*McIlwain*, 1975; *Moore et al.*, 1981]. For this reason we take $C = 0$ as our standard parameter, departing from the value reported by *Li et al.* [1998]. Still we vary this parameter to see the effect it has on the results of the model.

[51] We know of no particular observations for the radial width of the pulse, so we choose a broad range of parameters. Physically, however, it could neither be extraordinarily large or small, so we choose values between 5000 and 35,000 km.

[52] The other parameter, R_i , is an artifact of the model. The model requires that some initial position be given. Physically, it is not known how the compressional pulse is created or from what distance it originates. Because we are doing particle drift simulations, this parameter can affect the results. Electrons in the background magnetic field will drift and not wait for the pulse to arrive. In reality, before the pulse arrives one would expect a steady state situation regarding the existing electron distribution. There should not be any difference for the transport of the electron population, but we do not have a steady state model and we must consider the effects of that.

[53] Three different distributions of electrons are chosen so as to show that the results are independent of the chosen ensemble of electrons. The spatial range of the initial distribution was chosen to correspond more closely with the spatial region of the geomagnetic tail as compared with the previous section (Figure 10), that is, the range of $-18.75 R_E < Y < 18.75 R_E$, $-20.0 R_E < X \leq -7.5 R_E$, and the initial energy of each electron ranges from $5 \text{ keV} \leq W_0 \leq 200 \text{ keV}$. We choose in spatial steps of $\Delta X = \Delta Y = 0.3125 R_E$, $0.52083 R_E$, $1.5625 R_E$ and energy increments of 1 keV, 5 keV, and 5 keV. This corresponds to 98,0560, 68,160, and 7360 electrons, respectively.

[54] Figure 11, shows the maximum energization ($W_{\text{final}}/W_{\text{initial}}$) for those particles which enter and remain inside the geosynchronous region which is chosen to be less than $6.8 R_E$. We choose this subset of all electrons since we are interested in only those which could undergo further energization by other mechanisms in the inner magnetosphere. Figure 12 shows an example of an electron similar to Figure 3a which enters the geosynchronous orbit region but does not remain trapped in the inner magnetosphere. We have excluded such untrapped orbits. The set corresponding to 980,560 electrons is indicated with dotted lines, 68,160 is indicated with dashed lines, and 7360 is indicated with a solid line.

Table 1. Parameter Scans Used in Simulations

Parameter	Value
E_0 , mV/m	0.5, 1.0, 2.0, 3.0, 4.0, 5.0
v , km/s	10, 50, 100, 200, 500
p	1.0, 2.0, 4.0, 8.0, 16.0, 32.0, 48.0, 64.0
d , km	5000, 10,000, 16,000, 25,000, 35,000
C , R_E	0.0, 1.0, 4.0, 6.0, 10.0, 15.0, 20.0
R_p , R_E	10, 20, 30, 40, 50

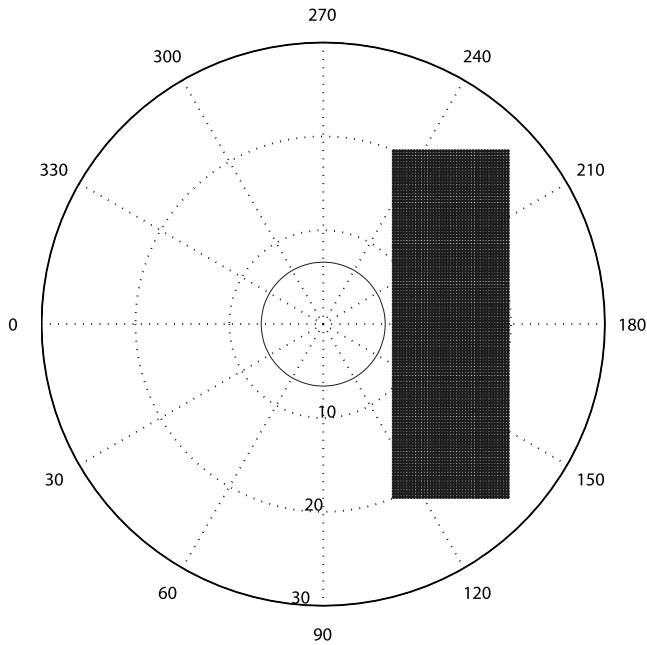


Figure 10. The spatial region for simulations of kappa distribution particles was chosen to correspond more closely with the spatial region of the geomagnetic tail, that is, the range of $-18.75 R_E \leq Y \leq 18.75 R_E$, $7.5 R_E \leq -X \leq 20.0 R_E$ in spatial steps of $\Delta X = \Delta Y = 0.3125 R_E$. The initial energy of each electron ranges from $5 \text{ keV} \leq W \leq 200 \text{ keV}$. In other simulations, spatial steps of 0.52083 and 1.5625 were used, but are not shown here. The circle is marked at $6.8 R_E$ as reference and to indicate the trapping region.

[55] We also show in Figure 13, the ratio of electrons that reach the geosynchronous region (again defined to be $L < 6.8$) to the initial electron population. This is an important indicator of the effectiveness of the substorm model in convecting tail particles earthward into the trapping area. Figure 14.

[56] One must note that the percentage shown here is dependent on what is selected as the initial distribution of particles, i.e., there are statistical fluctuations associated with the distribution we choose. Therefore what these ratios indicate is the relative effectiveness of the parameters and not either the number of plasma sheet particles or an absolute percentage that can be transported to the inner magnetosphere. However, since we consider such a broad sampling of the spatial and energy distribution and simulations show that the results are mostly independent of this sampling, we use these results as an absolute percentage to estimate properties of the plasma sheet.

[57] The implications for the varying the parameter E_0 is clear from Figures 11a and 13a. We note again that the maximum electric field strength is given by $E_0 \cdot 2^p$. Although increasing the electric field strength clearly energizes the particles more, the maximum number of simulated electrons trapped is 40% at $E_0 = 3.0 \text{ mV/m}$. The energization increases from roughly 10 for $E_0 = 0.5 \text{ mV/m}$ to 250 for $E_0 = 5.0 \text{ mV/m}$. This would be consistent with the single electron orbits of Figure 4a, which show that increasing the electric field causes the electron to gain energy.

[58] Figure 11b shows that energization with changing velocity v_0 is well correlated with the percent of electrons

convected to geosynchronous orbit. Very slow (10 km/s) and very fast (greater than 200 km/s) pulses are not effective in transporting a high injected flux from the plasma sheet. Both the energy gain in Figure 11b and the fraction of transported electrons in Figure 13b are maximum at 50 km/s. This is in agreement with other measurements [Russell and McPherron, 1973; Moore et al., 1981]. Moore et al. [1981] postulate that the low propagation speed can be explained by oxygen loading from the ionosphere. The single electron orbits of Figure 4b show similar results.

[59] One must take care in interpreting changes to the longitudinal width parameter p as the maximum electric field amplitude increases with increasing p while decreasing the longitudinal width as in (7). As this is the case, in order to separate the effect of the longitudinal pulse width by itself, the electric field parameter in Figures 11c and 13c is taken to be $E_0/2^p$ with $E_0 = 4.0 \text{ mV/m}$ in order to make comparisons with the other simulation in which $E_0 = 0.5 \text{ mV/m}$ and $p = 3$, giving a maximum field amplitude of 4.0 mV/m . Figures 11c and 13c indicate that smaller longitudinal widths or larger parameter p have larger energization, although the total number of transported electrons is much smaller. It would be expected that in a wider pulse the particle is under the influence of the electric field for a longer time, so the energization there should be higher. However, we look at that portion of the population that gets trapped, and since it is very easy for electrons to drift out of the electric field, the electron population that is transported sees a stronger electric field on average and is energized more when the pulse is narrow. However, the total size of this population is very small, as indicated in Figure 13c. The single particle orbits, shown in Figure 4c, verify that it is much easier for an electron to stay in the electric field for a wider pulse than a narrower pulse.

[60] Larger radial pulse widths also energize electrons better due to the fact that they stay in a region of larger electric field longer, and larger pulse widths, controlled by the parameter d , are better at transporting larger numbers of particles as well. This is indicated in Figures 11d and 13d. Figure 4d would lead to a similar conclusion.

[61] Figures 11e and 13e show that increasing longitudinal delay parameter, C , above $6 R_E$ dramatically increases energization but only moderately increases the transport of particles. This behavior is most easily understood by reference to the single electron orbits of Figure 4f. With a larger value of C , the electron is able to see an electric field at different times in its orbit (Figures 4f and 4g with $C = 20.0 R_E$) so the integrated electric field is large, rather than only once (Figures 4f and 4g with $C = 1.0 R_E$).

[62] The optimum initial radial position, R_i , of the pulse according to Figures 11f and 13f is $\sim 20\text{--}30 R_E$. We repeat that this parameter is a numerical artifact only; no definitive statements about the physical origin of the pulse in the tail can be made. As the initial starting point of the pulse is increased, many fewer electrons are trapped. This is most likely because many electrons have time to ∇B drift away before the pulse arrives. This is consistent with Figure 4e.

[63] We can then calculate the flux transported to geosynchronous orbit from the tail as follows. Equation (15) tells how the flux at geosynchronous orbit is related to the

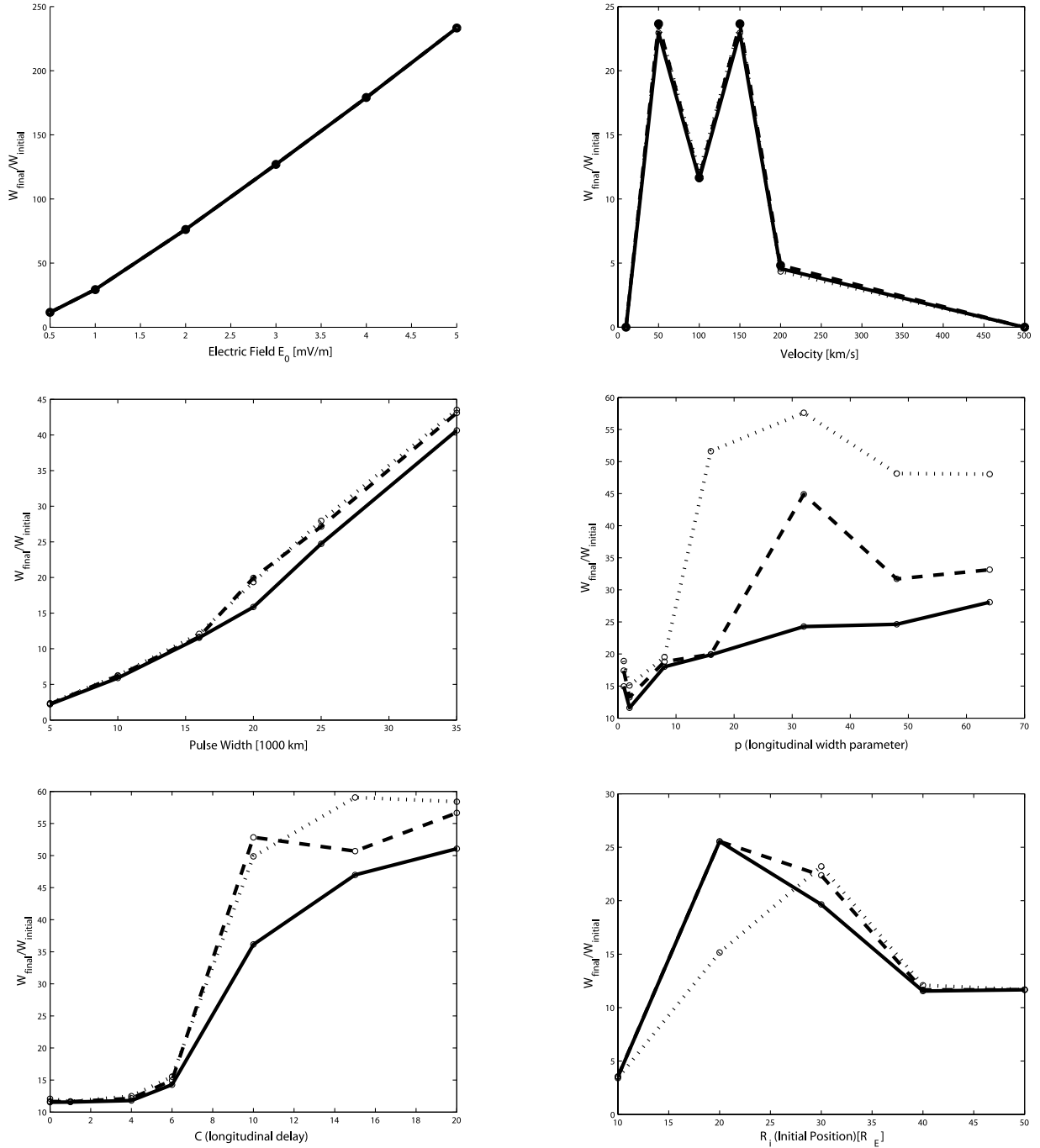


Figure 11. The maximum ratio of final energy to initial energy, $W_{\text{final}}/W_{\text{initial}}$, for electrons that reach the geosynchronous region (defined to be $L < 6.8$) from the initial tail distribution. The set corresponding to 980,560 electrons is indicated in black dots, 68,160 in black dashes, and 7360 in the solid black line. The electron orbits are computed for pulse parameters of $\mathbf{P} = E_0 = 0.5$ mV/m, $d = 16,000$ km $\approx 2.5 R_E$; $p = 3$; $v_0 = v_d = 100$ km/s; $A = 1$; $C = 0.0 R_E$; $R_i = 40.0 R_E$; $\phi_0 = 180.0$ as baseline parameters, while varying each of the other parameters separately.

ratio of final to initial energy and the initial flux. We have computed using simulations the percentage plasma sheet particles transported; therefore we can say that

$$j_f(W_f) = \left(\frac{W_f}{W_i} \right)_{\max} j_i(W_i) * \frac{\text{number of electrons with energy } W_i \text{ trapped}}{\text{total number of electrons with energy } W_i}. \quad (18)$$

The initial flux $j_i(W_i)$ was shown in Figure 5. Figure 18 shows the flux in the region of geosynchronous orbit for the different parameter scans we have done. Both *Kim et al.* [2000] and *Ingraham et al.* [2001] indicate a typical 1 MeV electron flux of $100 \text{ cm}^{-2} \text{ s}^{-1} \text{ sr}^{-1} \text{ keV}^{-1}$ following strong storms. The results of the flux transported to within geosynchronous orbit clearly show that the plasma sheet

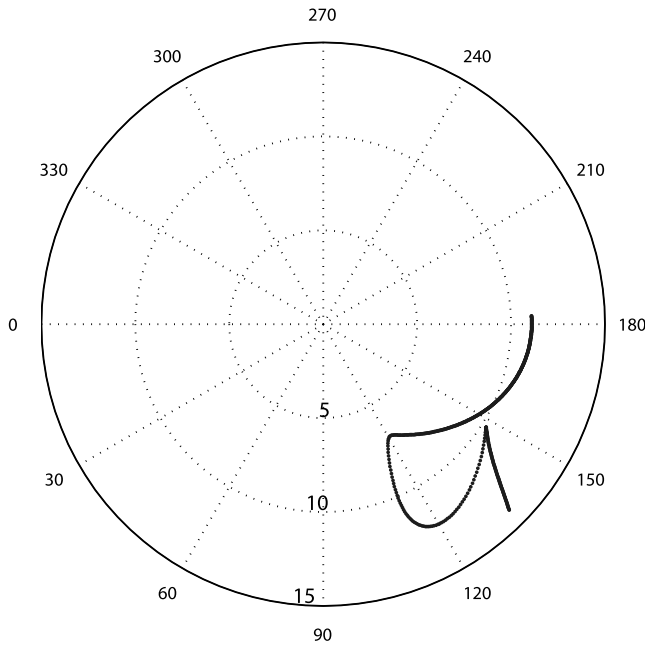


Figure 12. This shows an example of an electron orbit similar to Figure 3a which enters the geosynchronous orbit region but does not remain trapped; we have not included such orbits for this calculation since the electron does not remain within $L = 6.8$. We reason that such an electron could be detected during an injection event, but would not be energized to relativistic energies by other means. The parameters chosen for this orbit are also similar to Figure 3a. $\mathbf{P} = E_0 = 0.5$ mV/m; $d = 16,000$ km $\approx 2.5 R_E$; $p = 3$; $v_0 = 100$ km/s; $A = 1$; $C = 0.4$; $R_i = 40.0 R_E$ $\phi_0 = 180.0$ with similar initial conditions $R_0 = 14.0 R_E$, $\phi_0 = 135.0^\circ$, $W_0 = 25$ keV.

electrons, with energies less than 200 keV, are enough to account for the relativistic electrons.

[64] On the basis of these results, it is puzzling that enhancement of MeV electrons is not seen during substorms and is usually seen a few days following storms. It was proposed by *Ingraham et al.* [2001] that the large MeV electron curvature and ∇B drift velocity removes these electrons rapidly from the detector region and thus are not seen. Their velocity dispersion analysis indeed shows that MeV electrons as well as the lower-energy (<300 keV) electrons are both injected during substorm dipolarizations. Typical loss process such as scattering into the loss cone could serve to remove the electrons. We do not claim, however, that substorms themselves, in general, produce all the high-energy electrons, only that at lower energies, there is sufficient flux enhancement to provide the source for the MeV electrons.

5. Conclusion

[65] The flux of relativistic electrons ($E > 1$ MeV) in the Earth's outer radiation belt ($3 < L < 7$) varies substantially during geomagnetic storms. Often the flux may fall by up to a few orders of magnitude at the beginning of the main storm phase and may rise to levels 10–100 times the initial values over the next 2–3 days during the recovery phase. It

is proposed that substorm injections can provide a seed population of electrons, such that other in situ acceleration mechanisms can energize this population to relativistic energies. *Meredith et al.* [2002] find that the gradual acceleration of electrons to relativistic energies during storms can be effective only when there are periods of prolonged substorm activity following the main phase of the storm. We show that substorm injections can provide a sufficient flux of electrons in the inner magnetosphere so that in situ acceleration mechanisms can be a viable mechanism for the creation of relativistic electrons after storms.

[66] The series of simulations performed here also confirm the principal findings of *Li et al.* [1998] that electromagnetic pulses, which are meant to model compressional waves of the form observed in substorms [*Russell and McPherron*, 1973; *Moore et al.*, 1981], transport electrons into the inner magnetosphere across the geosynchronous orbit. The model used here is a nine-parameter particle tracing model. The injection of these electrons is dispersionless and the flux of these electrons coincides with what is observed by satellites.

[67] We have performed a series of simulations for different energy intervals of the initial electron ensembles with various initial spatial configurations of the initial electron ensembles and scans over a wide range of the electromagnetic model pulse parameters. The pulse parameters that we are interested in are the electric field strength, the pulse velocity, the radial and longitudinal width, the longitudinal velocity or equivalently longitudinal delay, and initial pulse position.

[68] Single electron orbits, as shown in Figure 4, are instructive in gaining physical insight into what determines transport from the tail to the inner magnetosphere. However, these must be confirmed by doing multiparticle simulations. The most important properties in determining the hardness and intensity of the energetic electrons from the substorm dipolarization pulse are the earthward propagation velocity v_0 , longitudinal width of the pulse controlled by the p parameter, and strength of the electric and magnetic fields controlled by the E_0 parameter. The strength of the electric field is of course important as this gives the electrons its energy, but there is a limit to the effectiveness of convecting electrons. Initializing the pulse somewhere around $20 R_E$ also seems to give the most effective energization rather than initializing further down the tail, but again we repeat that this parameter is a numerical artifact of the model and not necessarily very physical.

[69] For the cases considered, we find that the flux of electrons transported from the plasma sheet trapped in the inner magnetosphere is sufficient to account for the flux of electrons greater than 1 MeV seen after some storms. The other electrons are lost to various regions including the dawnside and dayside magnetopause. Examples of the electron energization factor $W_{\text{final}}/W_{\text{initial}}$ are shown in Figure 11 and the corresponding fraction of the test particle ensemble that reaches the inner magnetosphere is shown in Figure 13. We claim (Figure 18) that a substorm dipolarization and electron injection can transport enough high-energy electrons to account for the high fluxes seen after storms.

[70] That large fluxes of high-energy electrons, i.e., electrons with energy greater than 1 MeV, are not seen

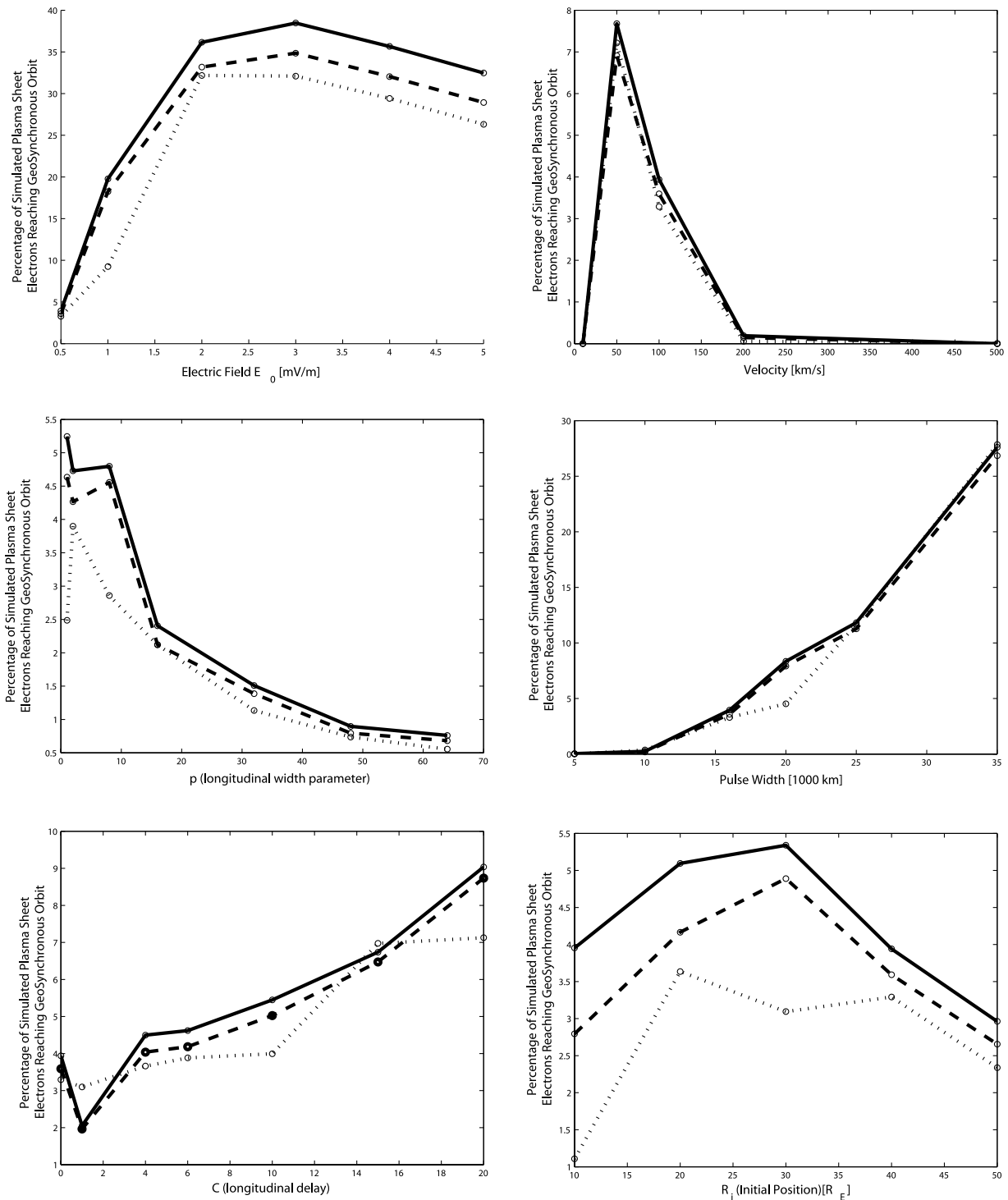


Figure 13. Percentage of electrons that reach the geosynchronous region (defined to be $L < 6.8$). The set corresponding to 980,560 electrons is indicated in black dots, 68,160 in black dashes, and 7360 in the solid black line. The electron orbits are computed for pulse parameters.

following substorms is not explained, although *Ingraham et al.* [2001] do make proposals. The influence of multiple substorm injections on storm time high-energy electrons requires a more comprehensive model of loss processes in the radiation belts, although it seems likely that this is an important factor.

[71] The simulations presented here lead to the conclusion that a low density of energetic, anisotropic ($T_{\perp} > T_{\parallel}$) electrons are injected into the inner magnetosphere by each dipolarization pulse. As in previous studies, we use only 90° pitch angle electrons, and future work would require a field model such that this restriction can be lifted. However, such

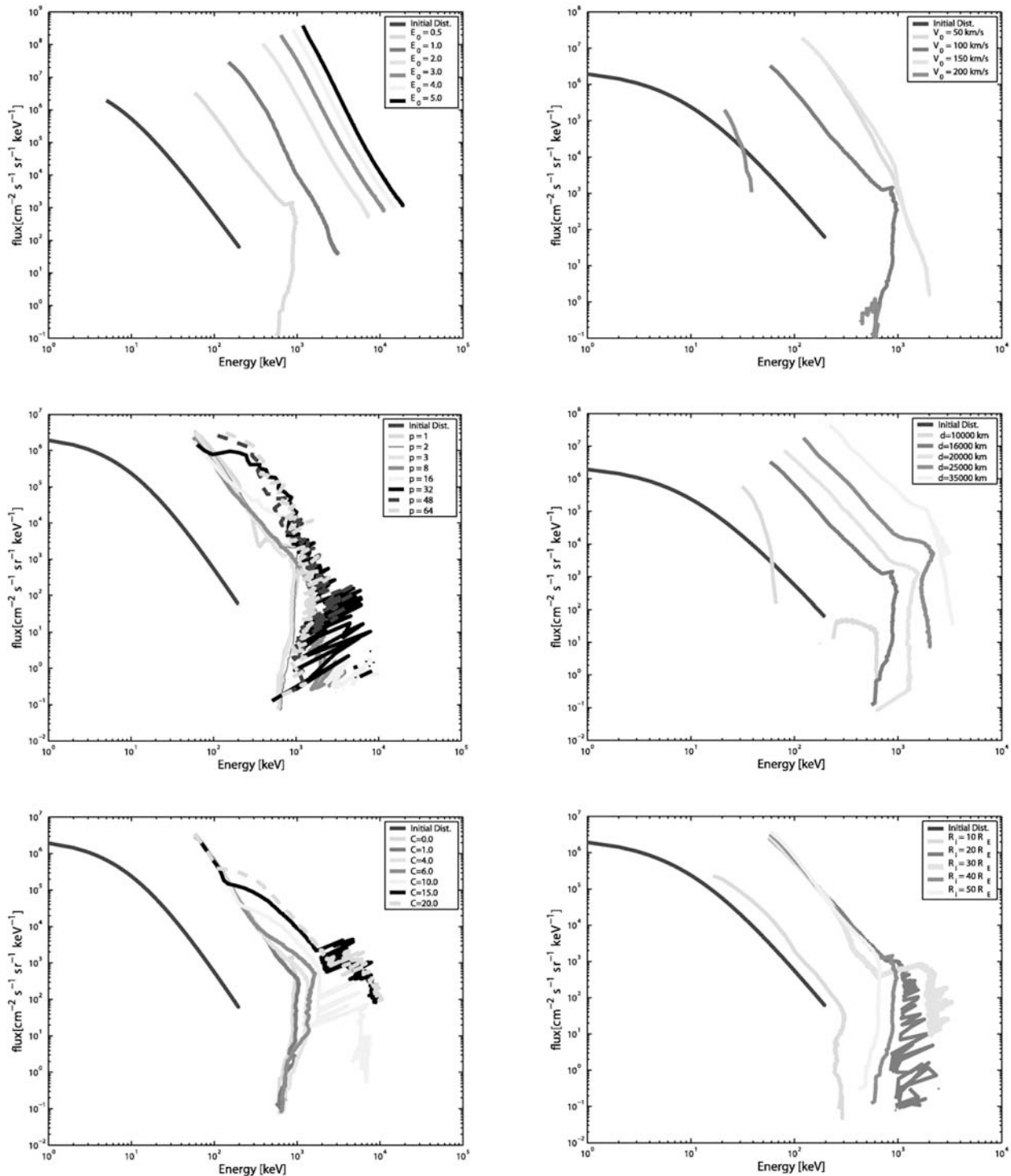


Figure 14. A comparison of the measured flux in the plasma sheet with the fluxes that can be obtained within geosynchronous orbit due to substorm injection. The initial flux is indicated in blue and is the same as Figure 5. The 1 MeV flux of electrons following a storm can be $100 \text{ cm}^{-2} \text{ s}^{-1} \text{ sr}^{-1} \text{ keV}^{-1}$. The flux of plasma sheet electrons below 200 keV transported during substorms is enough to account for the relativistic electrons. See color version of this figure at back of this issue.

anisotropic electron distributions drive whistler waves unstable [Gary, 1993], and whistler waves are widely observed in the postmidnight to morning sector of the inside the geosynchronous radius of the magnetosphere [Smith et

al., 1996]. Thus we suggest that an important next step in this problem is to couple these injected flux global test particle calculations to the local flux tube PIC simulations and quasilinear calculations for the nonlinear evolution of

whistlers fluctuations on the appropriate inner magnetosphere magnetic flux tubes. Using the simulations developed here as the injection source of higher-energy anisotropic electrons would be a new feature for whistler calculations. The whistler chorus is often involved as both a mechanism for scattering the electrons into the loss cone and as a mechanism for further hardening the energy of the medium-energy electrons to form the high-energy relativistic electrons.

[72] **Acknowledgments.** The authors give many thanks to Tom Moore and Xinlin Li for helpful discussions. This work was supported in part by the NSF grant ATM-0229863.

[73] Lou-Chuang Lee thanks Isidoros Doxas and another reviewer for their assistance in evaluating this paper.

References

- Aggson, T. L., J. P. Heppner, and N. C. Maynard (1983), Observations of large magnetospheric electron fields during the onset phase of a substorm, *J. Geophys. Res.*, *88*, 3981–3990.
- Arnoldy, R. L., and K. W. Chan (1969), Particle substorms observed at the geostationary orbit, *J. Geophys. Res.*, *74*, 5019–5028.
- Baker, D. N., P. R. Higbie, E. W. Hones Jr., and R. D. Belian (1978), High-resolution energetic particle measurements at 6.6 R_E : 3. Low-energy electron anisotropies and short-term substorm predictions, *J. Geophys. Res.*, *83*, 4863–4868.
- Baker, D. N., J. B. Blake, L. B. Callis, R. D. Belian, and T. E. Cayton (1989), Relativistic electrons near geostationary orbit: Evidence for internal magnetospheric acceleration, *Geophys. Res. Lett.*, *16*, 559–562.
- Baker, D. N., X. Li, J. B. Blake, and S. G. Kanekal (1998), Strong electron acceleration in the earth's magnetosphere, *Adv. Space Res.*, *21*, 609–613.
- Birn, J., M. F. Thomsen, J. E. Borovsky, G. D. Reeves, D. J. McComas, and R. D. Belian (1998), Substorm electron injections: Geosynchronous observations and test particle simulations, *J. Geophys. Res.*, *103*, 9235–9248.
- Cayton, T. E., R. D. Belian, S. P. Gary, T. A. Fritz, and D. N. Baker (1989), Energetic electron components at geosynchronous orbit, *Geophys. Res. Lett.*, *16*, 147–150.
- Christon, S. P., D. J. Williams, D. G. Mitchell, C. Y. Huang, and L. A. Frank (1991), Spectral characteristics of plasma sheet ion and electron populations during disturbed geomagnetic conditions, *J. Geophys. Res.*, *96*, 1–22.
- Daglis, I. A., R. M. Thorne, W. Baumjohann, and S. Orsini (1999), The terrestrial ring current: Origin, formation, and decay, *Rev. Geophys.*, *37*, 407–438.
- Delcourt, D. C., J. A. Sauvaud, and A. Pedersen (1990), Dynamics of single-particle orbits during substorm expansion phase, *J. Geophys. Res.*, *95*, 20,853–20,865.
- Fairfield, D. H., et al. (1998), Geotail observations of substorm onset in the inner magnetotail, *J. Geophys. Res.*, *103*, 103–117.
- Gary, S. P. (1993), *Theory of Space Plasma Microinstabilities*, Cambridge Univ. Press, New York.
- Ingraham, J. C., T. E. Cayton, R. D. Belian, R. A. Christensen, R. H. W. Friedel, M. M. Meier, G. D. Reeves, and M. Tuszewski (2001), Substorm injection of relativistic electrons to geosynchronous orbit during the great magnetic storm of March 24, 1991, *J. Geophys. Res.*, *106*, 25,759–25,776.
- Kamide, Y., et al. (1998), Current understanding of magnetic storms: Storm-substorm relationships, *J. Geophys. Res.*, *103*, 17,705–17,728.
- Kim, H. J., A. A. Chan, R. A. Wolf, and J. Birn (2000), Can substorms produce relativistic outer-belt electrons?, *J. Geophys. Res.*, *105*, 7721–7736.
- Kivelson, M. G., S. M. Kaye, and D. J. Southwood (1979), The physics of plasma injection events, in *Dynamics of the Magnetosphere*, p. 385, Springer, New York.
- Li, X., I. Roth, M. Temerin, J. R. Wygant, M. K. Hudson, and J. B. Blake (1993), Simulation of the prompt energization and transport of radiation belt particles during the March 24, 1991, SSC, *Geophys. Res. Lett.*, *20*, 2423–2426.
- Li, X., D. N. Baker, M. Temerin, D. Larson, R. P. Lin, D. Reeves, M. D. Looper, S. G. Kanekal, and R. A. Mewaldt (1997), Are energetic electrons in the solar wind the source of the outer radiation belt?, *Geophys. Res. Lett.*, *24*, 923–926.
- Li, X., D. N. Baker, M. Temerin, G. Reeves, and R. Belian (1998), Simulation of dispersionless injections and drift echoes of energetic electrons associated with substorms, *Geophys. Res. Lett.*, *25*, 3736–3766.
- Littlejohn, R. (1983), Variational principles of guiding center motion, *J. Plasma Phys.*, *29*, 111–125.
- Lyons, L. R., and D. J. Williams (1984), *Quantitative Aspects of Magnetospheric Physics*, Springer, New York.
- McIlwain, C. E. (1974), Substorm injection boundaries, in *Magnetospheric Physics*, edited by B. M. McCormac, p. 143, Springer, New York.
- McIlwain, C. E. (1975), Auroral electron beams near the magnetic equator, in *Physics of the Hot Plasma in the Magnetosphere*, edited by B. Hultquist and L. Stenflo, p. 91, Plenum, New York.
- McPherron, R. L. (1995), Magnetospheric dynamics, in *Introduction to Space Physics*, edited by M. G. Kivelson and P. T. Russell, Cambridge Univ. Press, New York.
- Meredith, N. P., R. B. Horne, R. H. A. Iles, R. M. Thorne, D. Heynderickx, and R. R. Anderson (2002), Outer zone relativistic electron acceleration associated with substorm-enhanced whistler mode chorus, *J. Geophys. Res.*, *107*(A7), 1144, doi:10.1029/2001JA900146.
- Moore, T. E., R. L. Arnoldy, J. Feynman, and D. A. Hardy (1981), Propagating substorm injection fronts, *J. Geophys. Res.*, *86*, 6713.
- Northrop, T. G. (1963), *The Adiabatic Motion of Charged Particles*, Wiley-Interscience, Hoboken, N. J.
- Russell, C. T., and R. L. McPherron (1973), The magnetotail and substorms, *Space Sci. Rev.*, *15*, 205.
- Sarris, T. E., X. Li, N. Tsaggas, and N. Paschalidis (2002), Modeling energetic particle injections in dynamic pulse fields with varying propagation speeds, *J. Geophys. Res.*, *107*(A3), 1033, doi:10.1029/2001JA900166.
- Shepherd, G. G., R. Bostrom, H. Derblom, C.-G. Falthammar, R. Gendrin, K. Kaila, R. Pellinen, A. Korth, A. Pedersen, and G. Wrenn (1980), Plasma and field signatures of poleward propagating auroral precipitation observed at the foot of the GEOS 2 field line, *J. Geophys. Res.*, *85*, 4587–4601.
- Smith, A. J., M. P. Freeman, and G. D. Reeves (1996), Postmidnight VLF chorus events, a substorm signature observed at the ground near $L = 4$, *J. Geophys. Res.*, *101*, 24,641–24,653.
- Tsyganenko, N. A., and D. P. Stern (1996), Modeling the global magnetic field of the large-scale birkeland current systems, *J. Geophys. Res.*, *101*, 27,187–27,198.
- Vasyliunas, D. J. (1968), A survey of low-energy electrons in the evening sector of the magnetosphere with OGO 1 and OGO 3, *J. Geophys. Res.*, *73*, 2839.
- Zaharia, S., C. Z. Zheng, and J. R. Johnson (2000), Particle transport and energization associated with disturbed magnetospheric events, *J. Geophys. Res.*, *105*, 18,471.

M. Mithaiwala and W. Horton, Institute for Fusion Studies, University of Texas at Austin, Austin, TX 78712, USA. (horton@mail.utexas.edu)

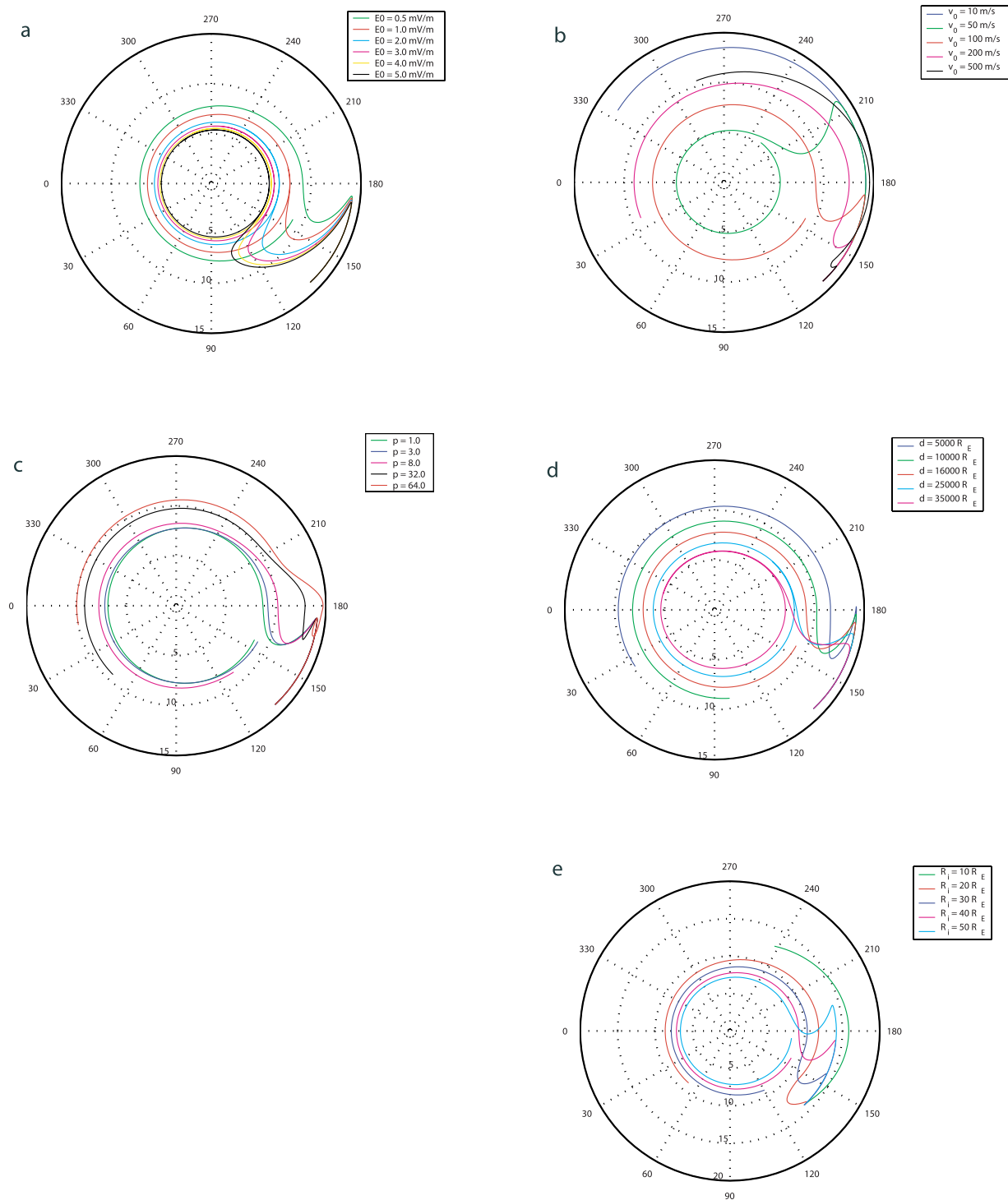


Figure 4. The electron orbit under different variations of the pulse parameters. The electron orbits are computed for pulse parameters of $\mathbf{P} = E_0 = 0.5$ mV/m, $d = 16,000$ km $\approx 2.5 R_E$; $p = 3$; $v_0 = v_d = 100$ km/s; $A = 1$; $C = 0.0 R_E$; $R_i = 40.0 R_E$; $\phi_0 = 180.0$ as baseline parameters, while varying each of the other parameters separately.

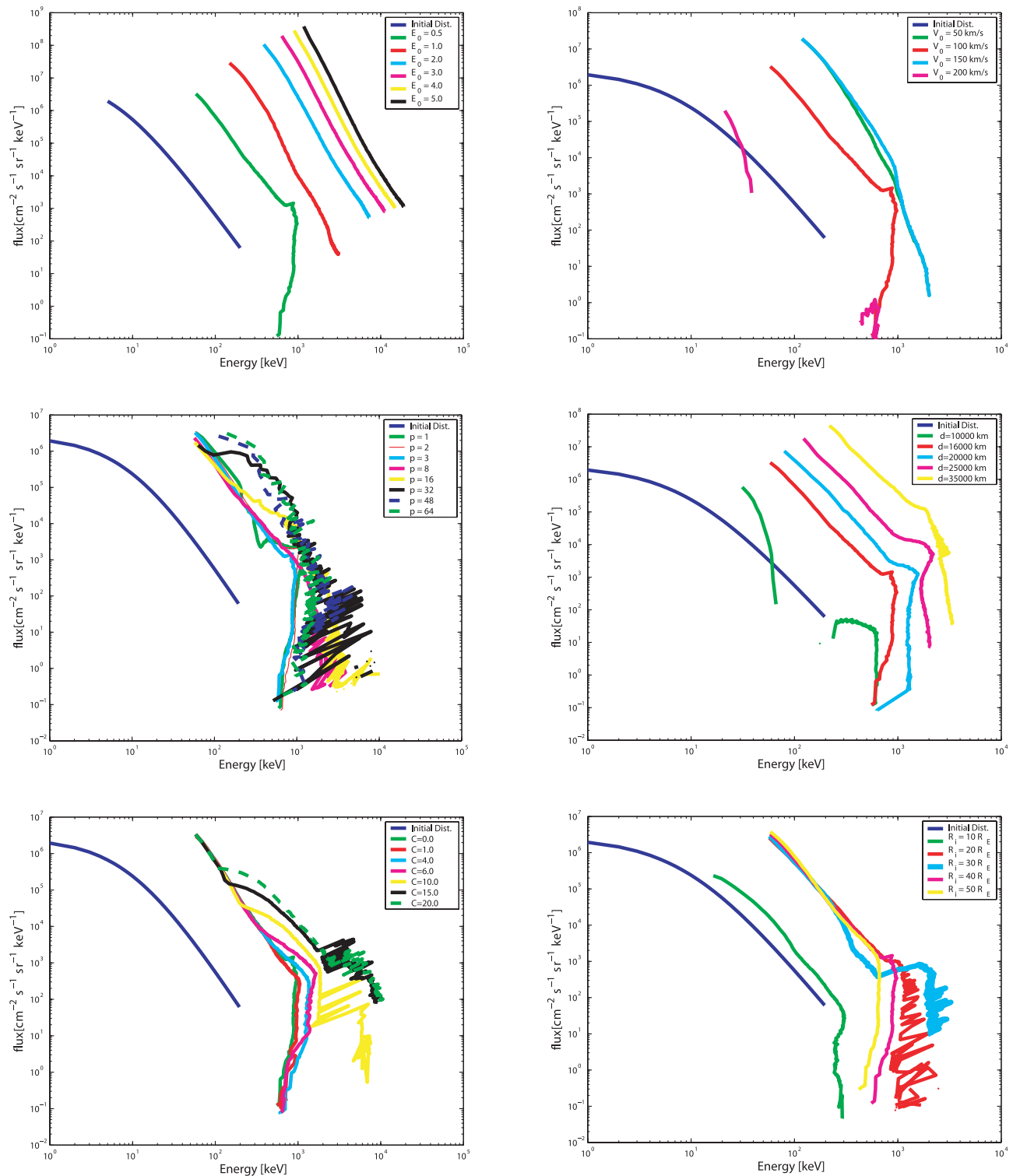


Figure 14. A comparison of the measured flux in the plasma sheet with the fluxes that can be obtained within geosynchronous orbit due to substorm injection. The initial flux is indicated in blue and is the same as Figure 5. The 1 MeV flux of electrons following a storm can be $100 \text{ cm}^{-2} \text{ s}^{-1} \text{ sr}^{-1} \text{ keV}^{-1}$. The flux of plasma sheet electrons below 200 keV transported during substorms is enough to account for the relativistic electrons.